$CaFe_2O_4$ ferrite nanofibers via solution blow spinning (SBS)

(Nanofibras de ferrita $CaFe_2O_4$ via solution blow spinning - SBS)

R. N. Araujo[1,2]*, E. P. Nascimento[1,2], H. B. Sales[1,2], M. R. Silva[3], G. A. Neves[2], R. R. Menezes[2]
[1]Federal University of Campina Grande, Materials Science and Engineering Graduate Program, Campina Grande, PB, Brazil
[2]Federal University of Campina Grande, Academic Unit of Materials Engineering, Campina Grande, PB, Brazil
[3]Federal University of Itajubá, Mechanical Engineering Institute, Itajubá, MG, Brazil

Abstract

$CaFe_2O_4$ nanofibers were successfully synthesized via solution blow spinning (SBS), and the influences of heat-treatment on morphological, microstructural, magnetic, and optical properties of the nanofibers were evaluated. In the synthesis process, stoichiometric amounts of iron and calcium nitrates were dissolved in an aqueous solution containing polyvinylpyrrolidone (PVP) and, after that, hybrid nanofibers (PVP/precursors) were produced by SBS. The hybrid nanofibers were calcined and then subjected to microstructural, morphological, and magnetic characterizations. The results evidenced that the fibers presented the crystalline nature of the single-phase $CaFe_2O_4$, with a crystallite size of 32.7 and 34.4 nm for the samples calcined at 800 and 1000 °C, respectively. The $CaFe_2O_4$ fibers calcined at 600 and 800 °C presented a homogeneous morphology, without beads, and mean diameters of 521 and 427 nm, respectively. The results also revealed nanofibers with low band gaps of approximately 1.98 eV and characteristics of soft magnetic materials.
Keywords: nanofibers, calcium ferrite, SBS.

Resumo

Nanofibras de $CaFe_2O_4$ foram sintetizadas com sucesso via solution blow spinning (SBS) e as influências do tratamento térmico nas propriedades morfológicas, microestruturais, magnéticas e óticas das nanofibras foram avaliadas. No processo de síntese, quantidades estequiométricas de nitratos de ferro e cálcio foram dissolvidos em solução aquosa contendo polivinilpirrolidona (PVP) e, em seguida, nanofibras híbridas (PVP/precursores) foram produzidas por SBS. As nanofibras híbridas foram calcinadas e depois submetidas às caracterizações microestrutural, morfológica e magnética. Os resultados evidenciaram que as nanofibras apresentaram natureza cristalina de fase única $CaFe_2O_4$, com tamanho de cristalito de 31,7 e 34,4 nm para as amostras calcinadas a 800 e 1000 °C, respectivamente. As fibras de $CaFe_2O_4$ calcinadas a 600 e 800 °C apresentaram morfologia homogênea, sem beads e com diâmetros médios de 521 e 427 nm, respectivamente. Os resultados também revelaram nanofibras com baixos gaps de energia de aproximadamente 1,98 eV e características de materiais magnéticos macios.
***Palavras-chave**: nanofibras, ferrita de cálcio, SBS.*

INTRODUCTION

Photocatalysts excited by visible light have been gaining prominence in recent researches due to their low-cost, high efficiency, and lack of secondary pollution in photodegradation processes [1, 2]. The band gap between valance and conduction bands is an important parameter that must be considered when selecting a photocatalytic material [3]. The sun emits light mainly in the visible spectrum, which accounts for 46% of the total energy. Hence, it is interesting that these materials exhibit a narrow band gap (<3.1 eV) to maximize the use of solar energy as an activation source in the photodegradation process [4]. Many photocatalysts (TiO_2, ZnS, $SrTiO_3$) possess large band gaps (>3.1 eV) and can use only a small portion of sunlight [5-7]. Ferrites have narrow band gaps that make them very efficient in visible light. Another advantage of ferrites is their magnetic properties, which enable their separation from the reaction mixture at the end of the process through an external magnetic field [8]. Calcium ferrite ($CaFe_2O_4$) has been largely investigated for photocatalytic applications because they possess a narrow band gap and, consequently, can absorb photons in the visible light range. This causes the excitation of electrons (e^-) from the valence band (VB) to the conduction band (CB) and generates electron holes (h^+). These photogenerated electron-hole pairs (e^-/h^+) are responsible for triggering a series of redox reactions, favoring the decomposition of organic compounds [9, 10]. To intensify the photocatalytic activity, photocatalysts have been synthesized with nanostructured morphology and dimensions. One-dimension nanostructures, such as nanotubes and nanofibers, provide high surface-to-volume ratio [11] and are less susceptible to agglomerate. Therefore,

**rondinele_nunes@hotmail.com*
https://orcid.org/0000-0002-1489-5285

they are considered more efficient alternatives when compared to nanoparticles.

Hence, calcium ferrite nanofibers synthesized via electrospinning [12, 13] have demonstrated an enhancement in photocatalytic activity due to their elevated surface area. Nevertheless, this technique has limitations concerning the use of high voltages and its low productivity, reducing the applicability on a large scale. To overcome the disadvantages of the electrospinning process, the solution blow spinning (SBS) technique was developed in 2009 [14]. The SBS method allows the production of polymeric and hybrid nanofibers on a large scale at a low-cost. Additionally, it is possible to obtain ceramic oxide nanofibers by using ceramic precursors, e.g., nitrates and acetates, during fiber preparation, coupled with the appropriate heat-treatment. Many studies have applied this methodology in the synthesis of ceramic nanofibers. It has been reported the fabrication of $YBa_2Cu_3O_{7-x}$ (YBCO) nanofibers by SBS followed by a two-stage heat-treatment: in the first stage, the samples were calcined at 450 °C for 3 h; in the second stage, the fibers were calcined at 820 °C for 14 h and then at 925 °C for 1 h [15, 16]. Superconducting $Bi_2Sr_2Ca_1Cu_2O_x$ (BSCCO) micro and nanofibers have been synthesized by SBS and a heat-treatment at 850 °C for 2 h [17]. Ni/CeO_2 nanofibers were prepared by applying the SBS method, followed by calcination at 800 °C for 1 h [18]. The SBS was used for the first time for the production of nickel ferrite nanofibers in 2018 [19] and, more recently, in 2019, for the preparation of MFe_2O_4 (M= Cu, Co, Ni) ferrite nanofibers [20]. However, there are no studies, so far, that has sought to apply the SBS process to the preparation of calcium ferrite nanofibers, despite the potential of this material as photocatalyst under visible light and the high production rate of the SBS technique. Thus, the present study aimed to synthesize calcium ferrite nanofibers via solution blow spinning and investigate the influence of heat-treatment on the microstructural, morphological, magnetic, and optical properties of these nanofibers.

MATERIALS AND METHODS

Materials: for the synthesis of $CaFe_2O_4$ ferrite, the following reagents were used: iron (III) nitrate nonahydrate [$Fe(NO_3)_3.9H_2O$, Sigma Aldrich, 98%], calcium nitrate tetrahydrate [$Ca(NO_3)_2{\cdot}4H_2O$, Sigma Aldrich, 99%], polyvinylpyrrolidone (PVP, MW=1300000 g/mol, Sigma Aldrich), acetic acid ($C_2H_4O_2$, Dinâmica, 99.7%), and deionized water.

Preparation of solutions: the preparation of the precursor solutions followed a methodology adapted from a previous study [20]. Stoichiometric quantities of iron (III) nitrate (0.2 M) and calcium nitrate (0.1 M) in a 2:1 molar ratio were added to a solvent mixture of acetic acid and water 2:1 volume ratio and mixed under constant stirring for 4 h. Subsequently, 12 w/v% of PVP was added to the above solution and kept under stirring until the complete solubilization of the polymer. *Preparation of fibers (solution blow spinning - SBS)*: during fiber preparation, the precursor solutions were transferred to a plastic syringe and force-fed through an inner-nozzle by applying constant air pressure. In this procedure, the path between the spinning nozzle (4) and the collector (6) was kept heated at about 60 °C by a tubular furnace set at 300 °C (5) to favor efficient solvent evaporation and to maintain fiber integrity in the collector (Fig. 1). The spinning parameters used in this study are presented in Table I.

Heat treatment: after the spinning process, nanofibers were kept in an oven for drying at 60 °C for 24 h. After that, they were calcined at 600, 800, and 1000 °C in two stages. In the 1st stage, fibers were heated from room temperature to 200 °C at a 3 °C/min heating rate with a residence time of 120 min. In the 2nd stage, the samples were heated from 200 °C to the final firing temperature at a 2 °C/min heating rate and with a residence time of 120 min. The purpose of the systematics used was to promote a porous structure without compromising the integrity of the nanofibrillar morphology. The final products were marked as CFO600, CFO800, and

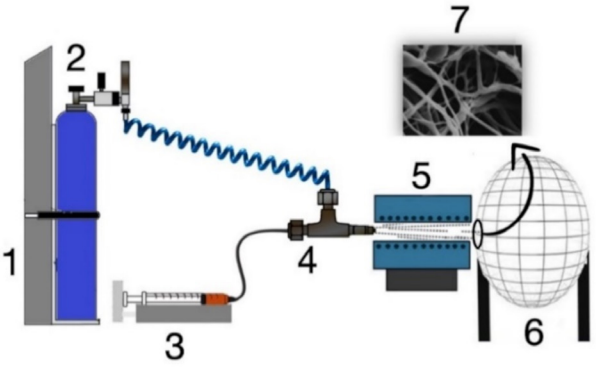

Figure 1: Spinning apparatus scheme: 1) air compressor; 2) pressure gauge; 3) injection pump; 4) concentric nozzles; 5) tubular furnace; 6) static collector; and 7) nanofibers.
[Figura 1: Esquema do aparato de fiação: 1) compressor de ar; 2) manômetro; 3) bomba de injeção; 4) bocais concêntricos; 5) forno tubular; 6) coletor estático; e 7) nanofibras.]

Table I - Parameters used during the spinning process (SBS).
[Tabela I - Parâmetros usados durante o processo de fiação (SBS).]

Parameter	Value
Diameter of the outer nozzle	1.8 mm
Diameter of the inner nozzle	1.0 mm
Protrusion distance of the inner nozzle	1.0 mm
Working distance	640 mm
Injection rate	4.5 mL/h
Air pressure	0.27 MPa
Temperature of the tubular furnace	300 °C
Diameter of the tubular furnace	75 mm
Length of the tubular furnace	520 mm
Temperature of collector	60 °C

CFO1000 for the samples calcined at 600, 800, and 1000 °C, respectively.

Characterization: the thermal decomposition behavior of the as-spun hybrid fibers (PVP/ceramic precursors) was studied by thermogravimetric (TG) analysis using a Shimadzu DTG-60H instrument. The samples were heated from 25 to 1000 °C under an oxidative atmosphere (synthetic air, 21% O_2+79% N_2) at a heating rate of 3 °C/min. The crystalline structure of the as-prepared nanofibers was investigated by X-ray diffraction (XRD-6000, Shimadzu) using a Ni-filtered CuKα radiation source (λ=1.5404 nm), with 2θ varying from 10° to 80°, a scan speed of 0.02 °/min, and a count time of 0.60 s. The average crystallite size was determined using the Scherrer equation. Fiber morphology was studied by scanning electron microscopy (SEM, SSX-550, Shimadzu); fiber diameter was measured for ~100 fibers using image analysis software (Image J, National Institutes of Health, USA). UV-vis diffuse reflectance spectra (DRS) were recorded in the spectral range of 200 to 800 nm in a spectrophotometer (UV-3600, Shimadzu), using an integrated sphere (ISR-3100, Shimadzu). Band gap (E_g) values were determined using the modified Kubelka-Munk equation:

$$[F(R).h.\nu]^n=B(h.\nu-E_g) \quad (A)$$

where R is the reflectance, F(R) is proportional to the absorption coefficient (α), B is a constant, h is the Plank's constant (J.s), and ν is the frequency of the light (s^{-1}). For the analysis, a $[F(R).h.\nu]^{1/2}$ versus photon energy (E=h.ν) graph was plotted, in which the interception between the extrapolated linear portion and the energy (E) axis provided the band gap energy of the fibers. The magnetic properties were studied using a vibrating sample magnetometer (VSM, mod. 7404, Lake Shore), with a maximum applied magnetic field of 15 kOe at room temperature.

RESULTS AND DISCUSSION

The thermogravimetric (TG) and derivative thermogravimetric (DTG) analysis of the fibers are shown in Fig. 2. The TG curve showed 6 main weight loss steps, which corresponded to 6 peaks in the DTG curve. The first weight loss step (~15.7%) occurred between room temperature and ~100 °C and was likely to be related to the release of moisture and residual solvent (water and acetic acid) [13, 21]. The following 4 weight loss events were overlapped and only distinguished in the DTG curve, which indicated that these reactions occurred at the same time. These loss steps together accounted for 50.5% of the total weight loss and occurred between 100 and 634 °C. They can be ascribed to the decomposition of nitrates from the inorganic precursors [22] and to the PVP decomposition [23]. Usually, PVP decomposes between 250 and 550 °C under an oxidizing atmosphere [24]. The presence of inorganic precursors may have displaced the decomposition of PVP to higher temperatures. The 6th step of about 25.1% of weight loss started at 634 °C and ceased at about 850 °C and can be ascribed to the decomposition of the remaining residual carbonaceous compounds from the PVP decomposition.

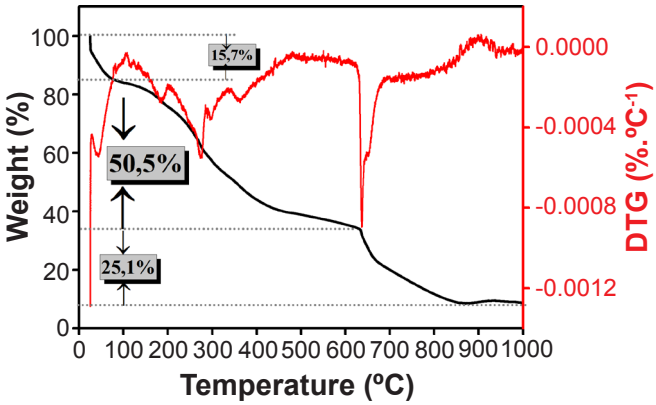

Figure 2: TG and DTG curves of the hybrid fibers obtained by SBS. *[Figura 2: Curvas de TG e DTG das fibras híbridas obtidas por SBS.]*

The morphology and diameter distribution of the calcium ferrite nanofibers calcined at different temperatures are shown in Fig. 3. The samples were constituted of randomly distributed fibers without beads. Beads are undesired spherical structures that resemble a pearl necklace. They occur during the spinning process due to solution instability that results from low viscosity [25]. The absence of beads in this study was related to the adequate viscosity of the solutions used in the spinning process. The resulting fibers were more uniform than the fibers prepared in other studies [15, 17]. The CFO600 nanofibers presented an average diameter of 520 nm and smooth surface (low rugosity) owing to the partial decomposition at 600 °C of the polymer used as spinning aid (Fig. 3a). There was a reduction of approximately 18% in the average diameter of the nanofibers with increasing calcination temperature to 800 °C (average diameter of 426 nm). The CFO800 nanofibers were composed of interconnected $CaFe_2O_4$ nanograins. These fibers possessed a rough surface and a highly porous structure due to the complete decomposition of the organic components in solution and a pre-sintering process (Fig. 3b).

Calcination at 1000 °C was sufficient to start the sintering process, which caused grain coalescence and resulted in the partial destruction of the nanofibrillar morphology (Fig. 3c). Similar behavior was reported in a study addressing $CaFe_2O_4$ nanofibers produced by electrospinning [12], in which a complete collapse of the nanofibrillar morphology was observed with increasing calcination temperature. This is an undesirable effect for applications in photocatalysis, where high surface area is sought. Nanofibers produced by SBS presented average diameters larger than the diameters of fibers prepared by electrospinning (average diameters around 200 nm) [13]. On the other hand, $CuFe_2O_4$, $CoFe_2O_4$, and $NiFe_2O_4$ nanofibers have been synthesized via SBS with average diameters of 200, 223, and 257 nm, respectively [20]. The larger fiber diameter found in this

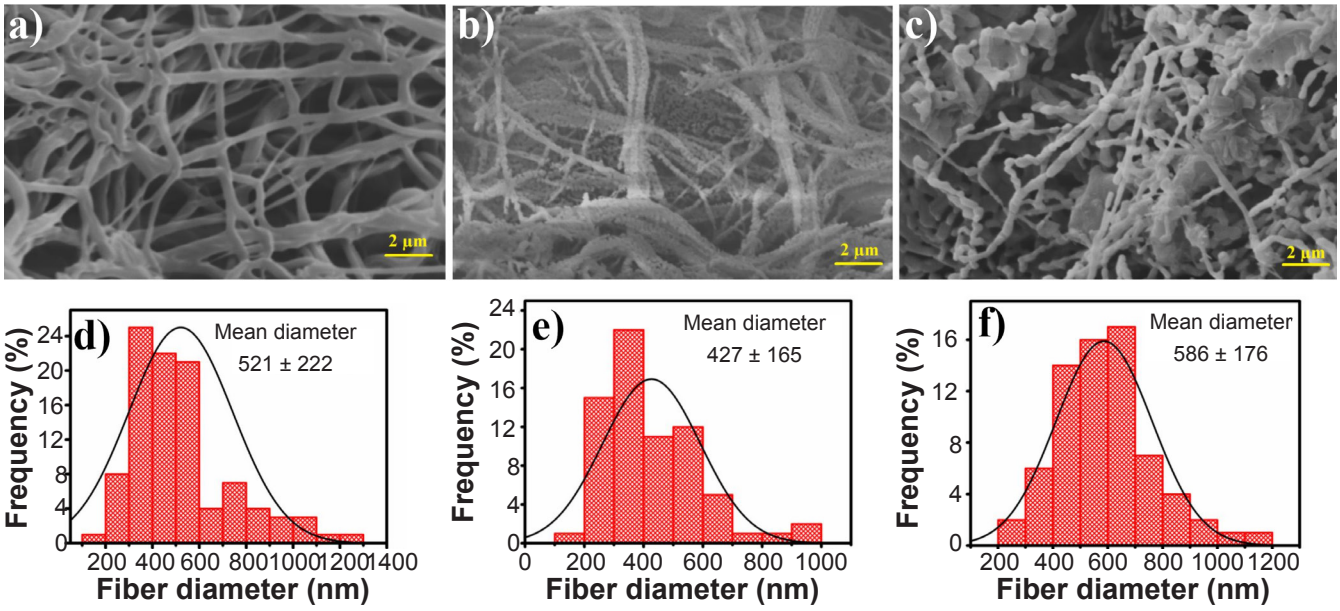

Figure 3: SEM micrographs (a-c) and diameter distribution graphs (d-f) of CFO600 (a,d), CFO800 (b,e), and CFO1000 (c,f).
[Figura 3: Micrografias de MEV (a-c) e gráficos de distribuição de diâmetro (d-f) de CFO600 (a,d), CFO800 (b,e) e CFO1000 (c,f).]

study can be explained first by the larger atomic radius of calcium incorporated in the lattice. This generates larger interconnected nanoparticles, which, in turn, produces thicker nanofibers at the end of the process [26]. The difference in fiber diameter also results from the conditions used in the SBS process. The air pressure used in the present study was approximately 0.27 MPa, while that used in [20] was 0.41 MPa. A higher pressure promotes greater elongation of fibers and, consequently, reduces their diameters. Furthermore, the use of a heated furnace during the spinning also contributed to larger diameters. The high temperature inside the tube caused rapid solvent evaporation and, therefore, faster solidification, which restricted even further fiber retraction. Such an effect would not be noticeable if no furnace was employed in the spinning process since the fibers formed and retained in the collector tend to have a high amount of solvent between polymer molecules. The trapped solvents promote greater fiber densification as they slowly evaporate. Finally, polymer content (spinning agent) is an important parameter when it is desired to obtain small diameter and defect-free nanofibers. For example, it was found that the addition of 10% BSCCO to the PVP solution (c=0.10 g/mL) results in homogeneous nanofibers with little imperfections and an average diameter of ~980 nm [17]. After adding 15% BSCCO, there was a decrease in the diameter to ~800 nm. By adding 20% BSCCO to the PVP solution, a large increase in morphological defects was observed due to the low viscosity of the solution and the lower evaporation of the solvent present in high concentration [17]. To avoid morphological imperfections caused by the low volatility of the solution due to the presence of water, acetates as precursors in a solution composed of a mixture of acids and ethanol were used [27]. However, the obtained YBCO fibers were entangled and highly irregular. This result suggests that just changing the solvent in the SBS process is not enough to obtain fine and defect-free nanofibers. Following the acetate route, it was tried to control the morphology of the nanofibers by changing the injection rate of the precursor solution (3.6, 4.8, and 6 mL/h), and an increase in the average fiber diameter (258, 562, and 984 nm) was observed due to increased injection rate [16].

XRD patterns of the calcium ferrite products are shown in Fig. 4. The CFO600 nanofibers did not present well-defined diffraction peaks, which indicated that 600 °C was insufficient for the formation of the desired phase, as also observed in the literature [12]. The CFO800 and CFO1000 samples showed well-defined peaks that were indexed to the orthorhombic structure of the $CaFe_2O_4$ phase (ICSD crystallographic file, JCPDS 29-1004). No secondary phases were observed, such as Fe_2O_3. A similar structure was reported in a study addressing the use of $CaFe_2O_4$ ferrite as electrochemical sensors [28]. With increasing temperature from 800 to 1000 °C, an increase in peak intensity was observed, favored by a greater degree of crystalline ordering. The CFO800 and CFO1000 nanofibers exhibited average crystallite sizes of 31.7±6.4 and 34.4±6.7 nm, respectively. Theoretically, crystallite size is related to the surface area. If the average crystal size is small, the surface area tends to be larger and, consequently, there are more catalytic sites for photocatalytic reactions to take place [29].

The absorbance spectra of the nanofibers are shown in Fig. 5a. There were significant photon absorption bands in the visible region for all fibers. The CFO600 sample showed absorption at about 729 nm, while CFO800 and CFO1000 showed absorption at approximately 668 nm. These results revealed that after the formation of the $CaFe_2O_4$ phase, the heat-treatment did not influence photon absorption significantly. Plots of $[F(R).h.\nu]^{1/2}$ versus photon energy ($E=h.\nu$) are shown in Fig. 5b. The CFO600, CFO800, and CFO1000 nanofibers presented band gap (E_g) values ranging

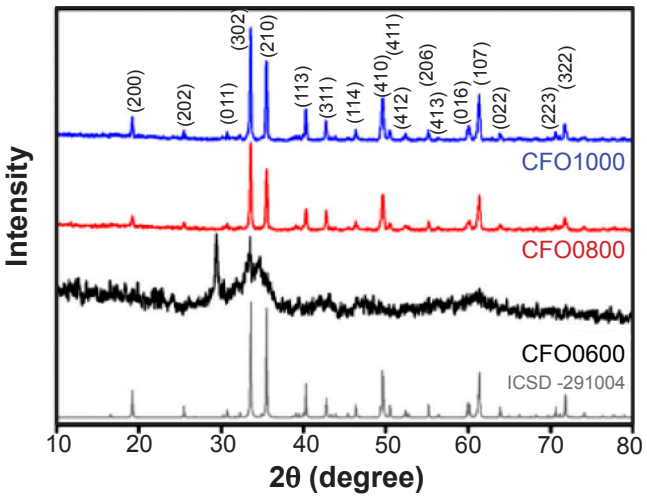

Figure 4: XRD patterns of $CaFe_2O_4$ nanofibers.
[Figura 4: Padrões de DRX das nanofibras de $CaFe_2O_4$.]

from 1.97 to 1.99 eV. The potentials of conduction (E_{CB}) and valence (E_{VB}) bands were calculated using the following empirical equations [30, 31]:

$$E_{VB}=X-E_e+0.5E_g \quad (B)$$

$$E_{CB}=E_{VB}-E_g \quad (C)$$

where X is the geometric mean of the absolute electronegativity of the constituent atoms (for $CaFe_2O_4$, X=3.69 eV), and E_e is the free electron energy on the hydrogen scale (4.5 eV). Therefore, the values of the potentials of the conduction band (CB) and valence band (VB) for the CFO800 product were -1.80 and 0.19 eV (vs. NHE), respectively. Similar results have been reported for $CaFe_2O_4$ nanoparticles with band gap values below 2.0 eV [9, 32, 33], which show potential for application in photocatalysis under visible light. The nanofibers produced in this study showed lower band gap energy values when compared to $Mg_{1-x}Zn_xFe_2O_4$ ferrites (band gaps in the range of 2.1 to 2.18 eV) [26], BiOCl nanoparticles (3.5 eV) [34], and NiO/ZnO nanocomposites (between 3.02 and 3.28 eV) [35]. These nanomaterials can be applied efficiently under UV radiation due to their slightly wide energy gaps, but do not have photocatalytic activity under visible light.

Magnetic hysteresis loops of CFO600, CFO800, and CFO1000 nanofibers are shown in Fig. 6. The curves of magnetization versus applied magnetic field showed that the $CaFe_2O_4$ nanofibers can be considered as soft ferromagnetic materials with practically negligible remanence and coercivity. The results also indicated that $CaFe_2O_4$ nanofibers exhibited superparamagnetic behavior [36], which is attributed to the effects of small grains in the nanofibers [37] and also to the non-magnetic character of the calcium ion. The magnetic contribution is dependent only on the distribution of the iron ions in the $CaFe_2O_4$ structure [38]. With the increase in calcination temperature from 600 to 800 °C, a decrease in saturation magnetization (M_s) from 8.27 to 1.58 emu/g was

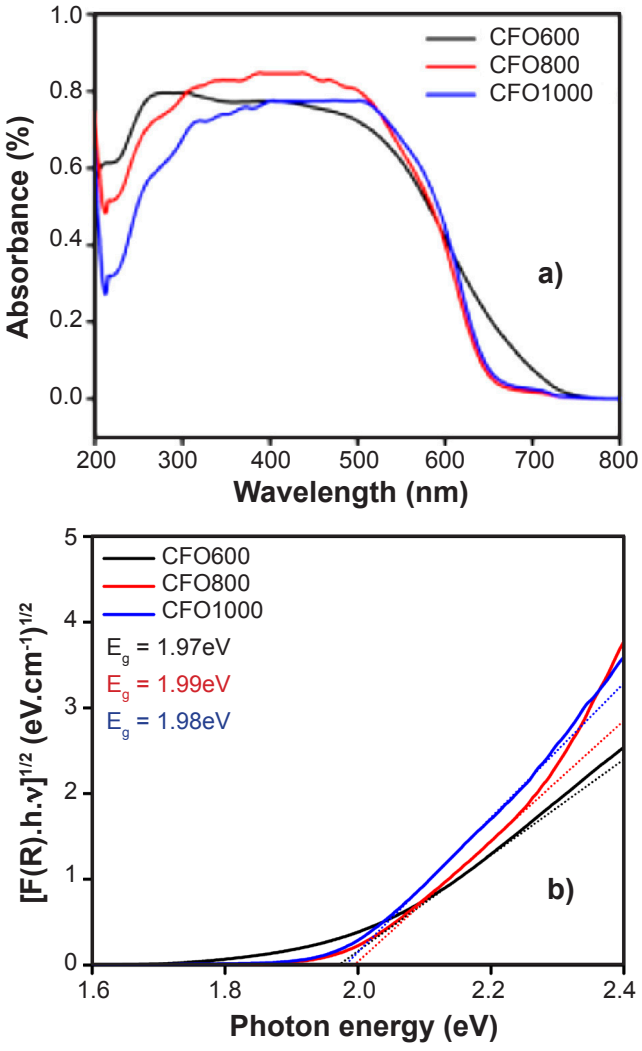

Figure 5: Absorbance spectra (a) and graphical representation of the Kubelka-Munk method (b) of $CaFe_2O_4$ nanofibers.
[Figura 5: Espectros de absorbância (a) e representação gráfica do método Kubelka-Munk (b) das nanofibras de $CaFe_2O_4$.]

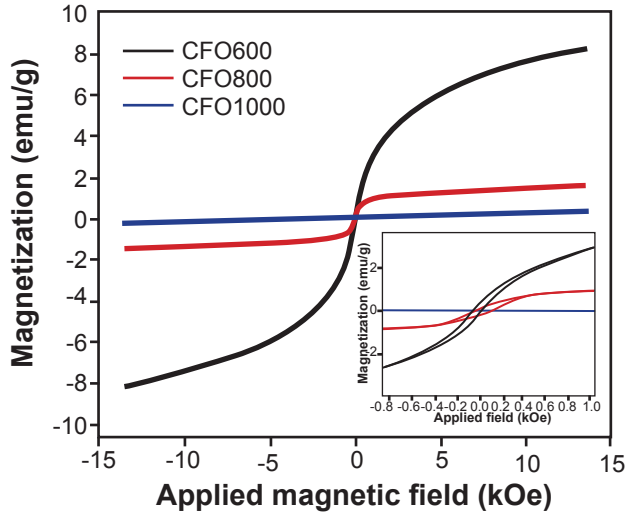

Figure 6: Magnetization hysteresis loops for $CaFe_2O_4$ nanofibers.
[Figura 6: Curvas de histerese de magnetização das nanofibras de $CaFe_2O_4$.]

observed. The CFO1000 nanofibers completely lost their magnetic character. Probably, the increase in calcination temperature caused an anti-parallel alignment of iron ions, canceling their magnetic moments in the nanofiber structure. Similar results have been reported, attributed mainly to the nanofiber morphology [12]. Temperatures above 800 °C caused structure collapse, resulting in loss of both dipolar and interfacial polarization. Also, such high temperatures increased anisotropy, which contributed to reduced magnetization. In general, superparamagnetic nanofibers are preferable for application in photocatalysis. This is because they can only aggregate and retain magnetization during the application of an external field. If the external magnetic field is withdrawn, this effect is ceased. Such behavior facilitates the separation process. In the present study, the prepared nanofibers showed very low remanence, which, in principle, should not affect their use in photocatalysis.

CONCLUSIONS

Monophasic calcium ferrite nanofibers were successfully synthesized via solution blow spinning. The results of X-ray diffraction and scanning electron microscopy indicated that the ideal calcination temperature is 800 °C for the formation of the $CaFe_2O_4$ phase without collapsing the nanofibrillar morphology. According to the results of UV-vis diffuse reflectance spectroscopy and vibrating sample magnetometry, calcium ferrite nanofibers show potential for application as photocatalysts under visible light due to their low band gap energy and superparamagnetic character. These features make possible their use and subsequent facile removal using an external magnetic field, maximizing their efficiency.

ACKNOWLEDGMENTS

The authors would like to express their thanks to the Coordenação de Aperfeiçoamento de Pessoal de Nível Superior (CAPES) for the student fellowship - Finance Code 001 (scholarship granted to Rondinele Nunes de Araujo) and to CNPq (grant nos. 308822/2018-8 and 420004/2018-1).

REFERENCES

[1] C. Lu, Z. Bao, C. Qin, L. Dai, A. Zhu, RSC Adv. **6** (2016) 110155.
[2] Y.R. Yao, W.Z. Huang, H. Zhou, H.Y. Yin, Y.F. Zheng, X.C. Song, Mater. Chem. Phy. **148** (2014) 896.
[3] S.-Q. Liu, Environ. Chem. Lett. **10** (2012) 209.
[4] E. Casbeer, V.K. Sharma, X.-Z. Li, Sep. Purif. Technol. **87** (2011) 1.
[5] S. Boumaza, A. Boudjemaa, A. Bouguelia, R. Bouarab, M. Trari, Appl. Energy **87** (2010) 2230.
[6] M. Kitano, M. Hara, J. Mater. Chem. **20** (2010) 627.
[7] S. Xu, W. Shangguan, J. Yuan, J. Shi, M. Chen, Sci. Technol. Adv. Mater. **8** (2007) 40.
[8] L. Machala, J. Tucek, R. Zboril, Chem. Mater. **23** (2011) 3255.
[9] A. Charles, C.K. Cheng, J. Environ. Manage. **234** (2019) 404.
[10] S. Ida, K. Yamada, T. Matsunaga, H. Hagiwara, Y. Matsumoto, T. Ishihara, J. Am. Chem. Soc. **132** (2010) 17343.
[11] Kenry, C.T. Lim, Prog. Polym. Sci. **70** (2017) 1.
[12] A. El-Rafei, A.S. El-Kalliny, T.A. Gad-Allah, J. Magn. Magn. Mater. **428** (2017) 92.
[13] X. Xu, S. Li, X. Wang, Y. Ma, X. Wang, K. Gao, Mater. Lett. **143** (2015) 75.
[14] E.S. Medeiros, G.M. Glenn, A.P. Klamczynski, W.J. Orts, L.H. Mattoso, J. Appl. Polym. Sci. **113** (2009) 2322.
[15] M. Rotta, L. Zadorosny, C. Carvalho, J. Malmonge, L. Malmonge, R. Zadorosny, Ceram. Int. **42** (2016) 16230.
[16] M. Rotta, M. Motta, A. Pessoa, C. Carvalho, W. Ortiz, R. Zadorosny, J. Mater. Sci. Mater. Electron. **30** (2019) 9045.
[17] C. Cena, G. Torsoni, L. Zadorosny, L. Malmonge, C. Carvalho, J. Malmonge, Ceram. Int. **43** (2017) 7663.
[18] T. Herminio, M.R. Cesário, V.D. Silva, T.A. Simões, E.S. Medeiros, D.A. Macedo, H.L. Tidahy, C. Gennequin, E. Abi-Aad, Environ. Chem. Lett. **18** (2020) 895.
[19] R.M.C. Farias, L.L. Severo, D.L. da Costa, E.S. de Medeiros, G.M. Glenn, L.N.L. Santata, G.A. Neves, R.H.G.A. Kiminami, R.R. Menezes, Ceram. Int. **44** (2018) 10984.
[20] V.D. Silva, L.S. Ferreira, T.A. Simões, E.S. Medeiros, D.A. Macedo, J. Colloid Interface Sci. **540** (2019) 59.
[21] S. Mohan, B. Subramanian, RSC Adv. **3** (2013) 23737.
[22] P. Melnikov, V.A. Nascimento, I.V. Arkhangelsky, L.Z. Zanoni Consolo, L.C.S. de Oliveira, J. Therm. Anal. Calorim. **115** (2013) 145.
[23] M.I. Loría-Bastarrachea, W. Herrera-Kao, J.V. Cauich-Rodríguez, J.M. Cervantes-Uc, H. Vázquez-Torres, A. Ávila-Ortega, J. Therm. Anal. Calorim. **104** (2010) 737.
[24] C. Peniche, D. Zaldívar, M. Pazos, S. Páz, A. Bulay, J.S. Román, J. Appl. Polym. Sci. **50** (1993) 485.
[25] A. Santos, M. Mota, R. Leite, G. Neves, E. Medeiros, R. Menezes, Ceram. Int. **44** (2018) 1681.
[26] N. Ghazi, H.M. Chenari, F. Ghodsi, J. Magn. Magn. Mater. **468** (2018) 132.
[27] M. Rotta, D.K. Namburi, Y. Shi, A.L. Pessoa, C.L. Carvalho, J.H. Durrell, D.A. Cardwell, R. Zadorosny, Ceram. Int. **45** (2019) 3948.
[28] P. Balasubramanian, R. Settu, S.-M. Chen, T.-W. Chen, G. Sharmila, J. Colloid Interface Sci. **524** (2018) 417.
[29] J. Gómez-Pastora, S. Dominguez, E. Bringas, M.J. Rivero, I. Ortiz, D.D. Dionysiou, Chem. Eng. J. **310** (2017) 407.
[30] Y. Huang, X. Zhang, G. Zhu, Y. Gao, Q. Cheng, X. Cheng, Sep. Purif. Technol. **215** (2019) 490.
[31] X. Li, T. Wan, J. Qiu, H. Wei, F. Qin, Y. Wang, Y. Liao, Z. Huang, X. Tan, Appl. Catal. B Environ. **217** (2017) 591.
[32] Y. Chen, Q. Wu, J. Wang, Y. Song, J. Ind. Eng. Chem. **77** (2019) 171.
[33] S. Vadivel, D. Maruthamani, A. Habibi-Yangjeh, B. Paul, S.S. Dhar, K. Selvam, J. Colloid Interface Sci. **480** (2016) 126.

[34] Y. Sun, C. Shao, X. Li, X. Guo, X. Zhou, X. Li, Y. Liu, J. Colloid Interface Sci. **516** (2018) 110. [35] M.M. Sabzehmeidani, H. Karimi, M. Ghaedi, Appl. Organomet. Chem. **32** (2018) e4335.
[36] A.K. Das, R. Govindaraj, A. Srinivasan, J. Magn. Magn. Mater. **451** (2018) 526.
[37] X. Huang, J. Zhang, S. Xiao, T. Sang, G. Chen, Mater. Lett. **124** (2014) 126.
[38] G. Lal, K. Punia, S.N. Dolia, P. Alvi, S. Dalela, S. Kumar, Ceram. Int. **45** (2019) 5837.
(Rec. 25/01/2020, Rev. 02/06/2020, Ac. 16/06/2020)